Materials Advances

ROYAL SOCIETY OF CHEMISTRY

PAPER

View Article Online
View Journal | View Issue

Cite this: *Mater. Adv.*, 2024, 5, 2377

CeO_2-promoted Cu_2O-based catalyst sprayed on the gas diffusion layer for the electroreduction of carbon dioxide to ethylene†

A. Alarcón, *[ac] T. Andreu [ab] and C. Ponce de León [c]

Received 15th November 2023,
Accepted 19th January 2024

DOI: 10.1039/d3ma01009k

rsc.li/materials-advances

The development of efficient and selective catalysts for the carbon dioxide reduction reaction (CO_2RR) is crucial for sustainable energy and chemical synthesis. In this work, CeO_{2-y} (y = C (cubic) and R (rod)) was incorporated into Cu_2O nanocube electrocatalyst as a promoter for ethylene (C_2H_4) production. The results demonstrate that the catalyst with a loading of 5 wt% crystalline CeO_{2-C} exhibits competitive activity and stability for ethylene production compared to pristine Cu_2O. Under optimized reaction conditions of −250 mA cm^{-2} current density and 1 M KOH electrolyte, the Cu_2O–$5CeO_{2-C}$ catalyst achieved a faradaic efficiency (FE) of ∼53% for C_2H_4 production, while maintaining stability over a period of 120 minutes. In contrast, non-promoted Cu_2O exhibited a lower FE for C_2H_4 (∼38%) and experienced partial deactivation after 45 minutes. The characterization of the catalysts before and after the reaction revealed that the interaction between Cu_2O and CeO_{2-C} creates intrinsic sites (Cu^x–CeO_{2-x}; Cu^x = Cu^{2+}, Cu^+, and Cu^0) for the binding of CO_2 and H_2O molecules. Moreover, the Cu_2O–$5CeO_{2-C}$ catalyst outperforms other reported systems in terms of FE and partial current density for C_2H_4 production. It requires a lower potential (−0.98 V *vs.* RHE) to operate at the same electrolyte concentration. This finding highlights the promising nature of Cu_2O–$5CeO_{2-C}$ as an efficient and cost-effective catalyst for C_2H_4 production.

Introduction

The electrochemical carbon dioxide reduction reaction (CO_2RR) has attracted enormous interest due to its mild reaction conditions and potential to be used for renewable electricity storage via the production of synthetic fuels. Particularly, the CO_2RR to ethylene (C_2H_4) aiming at high current densities and faradaic efficiencies (FE) is intensively studied because of the extremely high industrial value and the need to transition away from fossil fuel C_2H_4 production.[1] Copper-based (Cu,[2–4] CuO[5–8] and Cu_2O[9–14]) electrodes are proven to be the most used heterogeneous catalysts that tend to produce hydrocarbons and oxygenate compounds with competitive activity. However, as multi-step electron and proton transfer processes are involved in C_2H_4 formation, hydrogen (H_2) and other by-products such as methane (CH_4) will inevitably be produced during electrolysis. Therefore, the design of efficient catalysis systems specific for the CO_2RR to ethylene with both high selectivity and high FE as well as low overpotential is highly desirable.

Various catalyst design strategies have been reported to effectively regulate the selectivity of the CO_2RR.[15–17] Notably, by altering the electronic structure of Cu-based catalysts by the addition of a second metal[18–20] or metal oxide promoter[21] phase provides a significant improvement for C_2H_4 production. Ceria (CeO_2) is widely used as a catalyst, support and promoter for a variety of heterogeneous catalytic reactions involving the hydrogenation of CO_2[22] due to its acid–base and unique redox properties of oxygen storage and release.[23] The size and shape modification, surface/face reconstruction, and faceting of ceria at the nanoscale level can offer an important tool to govern activity and stability in these reactions.[24] Furthermore, strong interaction between noble metals and ceria leads to their higher dispersion, electronic modifications and enhanced catalytic activity.[25]

Recently, the implementation of CeO_2 as a support material for the CO_2RR has been investigated by some researchers. For instance, a high methane (CH_4) faradaic efficiency (up to ∼54% at −1.2 V *vs.* RHE) over Cu/CeO_{2-x} nanocrystalline heterodimers was reported by S. Varandili *et al.*[26] In another

[a] *Facultat de Química, Universitat de Barcelona, Martí i Franquès, 1, Barcelona 08028, Spain. E-mail: a.alarcon@ub.edu*
[b] *Sustainable Electrochemical Processes, Universitat de Barcelona, 08028, Barcelona, Spain*
[c] *Electrochemical Engineering Laboratory, Energy Technology Research Group, Faculty of Engineering and Physical Sciences, University of Southampton, Highfield Campus, University Road, Southampton, SO17 1BJ, UK*

† Electronic supplementary information (ESI) available. See DOI: https://doi.org/10.1039/d3ma01009k

study, Cu/CeO_2 carbon nanofiber (Cu/CeO_x@CNF) catalysts synthesized by an electrospinning method were explored by X. Zong *et al.*[27] In this case, their optimized Cu/CeO_x@$CNF_{S\text{-}2}$ catalyst exhibited a high CO faradaic efficiency (up to ~59% at −0.6 V *vs.* RHE) at a high current density of 100 mA cm^{-2}. Most recently, Zhao *et al.*[28] have that the Cu electrode coating with CeO_2 nanoparticles largely enhanced the C_{2+} product selectivity during CO_2 electroreduction. The FE and partial current density of C_{2+} products on the CeO_2–Cu electrode achieved in a gas-tight H-type electrolytic cell with 0.1 M $KHCO_3$ was 61% and 8.45 mA cm^{-2} at −1.05 V *vs.* RHE, respectively. In that study, 1.5 mg cm^{-2} was found to be the optimal CeO_2 coating. The improved CO_2RR selectivity and activity of CeO_2–Cu were attributed to the interface between Cu and CeO_2, which promotes C–C coupling towards C_{2+} production products. The CO_2RR to C_{2+} has also been evaluated over a CuO modified 20 wt% CeO_2 catalyst using a flow cell at 1 M KOH. Under those conditions, the reported faradaic efficiency of the C_{2+} products was ~75.2% at a current density of 1.21 A cm^{-2}. S. Yan *et al.*[29] revealed that CeO_2 and Cu and the subsurface Cu_2O coexisted in CeO_2/CuO during the CO_2RR and two competing pathways for C–C coupling were promoted separately, of which hydrogenation of *CO to *CHO is energetically favoured.

In terms of the CO_2RR to C_2H_4, the stabilization of Cu^+ within a CuO–CeO_2 interface has been reported by S. Chu *et al.*[30] They suggested that tuning the CuO/CeO_2 interfacial interaction permits dramatic suppression of proton reduction and enhancement of CO_2 reduction. The C_2H_4 faradaic efficiency (up to ~50% at −1.1 V *vs.* RHE) was obtained over an optimised CuO/30 wt% CeO_2 using a liquid H-type cell with continuous CO_2 bubbling in 0.1 M $KHCO_3$ electrolyte. Lately, the effect of exposed facets of CeO_2 (cubes (100), rods (110), and octahedral (111)) has also been investigated under similar reaction conditions by S. Chu *et al.*[31] In the CeO_2-supported Cu nanoparticles, they found that CeO_2 changed the oxidation state of Cu atoms towards Cu^+ at the CuO–CeO_2 interface. This fact was mainly identified on the Cu/CeO_2(110), flowed by Cu/CeO_2(100) and Cu/CeO_2(111). The existence of Cu^+ species was supposed to be likely the adsorption and active sites for CO_2 activation followed by further C–C coupling to yield C_2H_4. The FE towards C_2H_4 was ~39% on the Cu/CeO_2(110) at a mild overpotential of 1.13 V. In another study performed on a flow-cell at high current density and under 1 M KOH, Ce-doped Cu nanoparticles (Ce–Cu NPs) were reported to be highly selective to C_2H_4. A high faradaic efficiency (FE) of C_2H_4 close to 53% at a current density of 150 mA cm^{-2} was achieved using a Ce/(Cu + Ce) precursor ratio = 10%. J. Shan *et al.*[32] suggested that the high performance, which is 2.8 times higher than Cu nanoparticles under the same conditions, is due to the shrinking of the particle sizes due to Ce doping resulting in more catalytic active sites with oxygen defects. It seems that the proximity of the Ce atoms can boost the local electronic distribution on the Cu nanoparticles. Under similar reaction conditions, anchoring CeO_2 quantum dots on to the CuO surface has been evaluated by S. Wang *et al.*[33] Their optimal catalyst consisting of 100 wt% CeO_2 and 50 wt% CuO achieved a high faradaic efficiency of ~50% for ethylene with a partial current density of 197 mA cm^{-2}, attributed to the CuO/CeO_2 interfaces that simultaneously stabilize Cu^+ and key intermediates.

Despite these advances in CuO supported CeO_2 electrocatalysts for CO_2RR to C_2H_4, the role of the CeO_2 as a promoter using Cu_2O instead of CuO has not been investigated yet. Recent studies have revealed that the Cu_2O phase provides a higher selectivity to ethylene compared to CuO.[34] Furthermore, the economic viability of most large-scale chemical processes relies on the use of simple and low-cost catalytic materials. Therefore, the implementation of CeO_2 as a promoter instead of bulk support is a practical way to design cost-effective electrocatalytic materials. In this line, the promoter content optimization into Cu_2O can provide a highly active-stable, and low-cost electrocatalytic formulation for C_2H_4 production.

Here, we developed a CeO_2-promoted Cu_2O-based catalyst sprayed on a carbon-based gas diffusion layer for the CO_2RR to C_2H_4. A series of Cu_2O–$xCeO_2$ were synthesized by the simple liquid phase reduction method. The influence of CeO_2 crystallinity and promoter loading (x = 5–20 wt%) was studied under relevant reaction conditions (current density (j) = −[50–300] mA cm^{-2}, 1 M KOH, and flow of CO_2 (F_{CO_2}) = 200 mL min^{-1}). Furthermore, the influence of the KOH concentration (0.1–3 M) and electrolyte type (KOH, KCl, and $KHCO_3$,) over the optimized Cu_2O–5CeO_2 GDE was investigated to identify the best reaction components. Lastly, its stability was additionally tested under the selected reaction conditions (j = −250 mA cm^{-2}, electrolyte = 1 M KOH, and F_{CO_2} = 200 mL min^{-1}). The physico-chemical properties responsible for catalyst performance were studied using scanning electron microscopy-energy dispersive X-ray spectroscopy (SEM-EDX), transmission electron microscopy (TEM), X-ray diffraction (XRD), and Raman and photoelectron spectroscopy (XPS).

Experimental section

Chemicals and reagents

All chemical reagents used were of analytical grade without further treatment. Copper(II) sulfate [$CuSO_4$, 99%] and Nafion® perfluorinated resin solution (5 wt% in a mixture of lower aliphatic alcohols and water, 45% water) were purchased from Sigma Aldrich. Cerium(III) nitrate hexahydrate [$Ce(NO_3)_3{\cdot}6H_2O$, 99.5%] was purchased from Thermo Scientific. L(+)-Ascorbic acid [$C_6H_8O_6$, 99%] was purchased from Acros Organics. Sodium hydroxide [NaOH, 97%], potassium hydroxide [KOH], and ethanol absolute [C_2H_6O, 99.8%] were purchased from Fisher Scientific. Ultrapure water was provided by Milli-Q Millipore source (18.2 MΩ cm, 20 °C).

Preparation of the catalysts

The promoter phase, CeO_2, was first synthesized using a hydrothermal method. In a typical synthesis, 3.25 g of $Ce(NO_3)_3{\cdot}6H_2O$ was dissolved in 15 mL of deionized water to obtain cerium nitrate aqueous solution. Then, a NaOH aqueous solution was prepared in a Teflon-lined steel reactor using 9 g

of NaOH and 50 mL of deionized water. The cerium nitrate aqueous solution was later added dropwise into the NaOH aqueous solution. After magnetic stirring for 30 min, the reactor was sealed and heated at two different temperatures of 80 °C and 240 °C for 24 h to obtain rod (R) and cubic (C) ceria particles, respectively. After cooling down to room temperature, the resulting precipitate was separated by centrifugation (4000 rpm for 5 min) and washed three times with excess ethanol, followed by drying in an oven overnight at 80 °C.

The series of CeO_2-promoted Cu_2O (Cu_2O–$x CeO_{2\text{-}y}$; x = 5, 10, 15 and 20 wt% and y = rod (R) and cubic (C) shape) samples were synthesized using a simple liquid phase reduction method. $CuSO_4$ (0.2689 g) and the respective amount of the promoter (CeO_2) were dissolved into 50 mL of distilled water under sonication for 30 min and later by magnetic stirring for 30 min. Sequentially, 0.8 g NaOH was dissolved in 50 mL of distilled water and added to the mixture dropwise. In the next step, 0.7045 g of $C_6H_8O_6$ as a reducing agent, was added to the mixture and kept constantly stirring for 30 min. Then, the CeO_2-promoted Cu_2O catalysts were centrifuged at 4000 rpm for 5 min and washed three times with excess ethanol. Finally, they were dried overnight in an oven at 80 °C. A non-promoted Cu_2O was also synthesized using the same procedure.

Preparation of gas diffusion electrode (GDE)

The GDE usually consists of a gas diffusion layer (GDL) on which a catalytic layer is deposited. The carbon-based GDL (Freudenberg H23C6) was used as the support. A catalytic ink was formulated by mixing 20 mg of the as-prepared catalyst, 0.5 mL of ethanol absolute and 140 μL of Nafion® perfluorate. The ink deposition on the GDL was performed using the spray coating technique. The catalyst loading mass was fixed to 1 ± 0.05 mg cm^{-2} according to the previous control test, see Fig. SI1 (ESI†). After the catalyst deposition, GDEs were dried at room temperature. The GDEs were denoted as Cu_2O, Cu_2O–$5CeO_{2\text{-}C}$, Cu_2O–$10CeO_{2\text{-}C}$, Cu_2O–$15CeO_{2\text{-}C}$, Cu_2O–$20CeO_{2\text{-}C}$, $CeO_{2\text{-}C}$, Cu_2O–$5CeO_{2\text{-}R}$, and $CeO_{2\text{-}R}$. Fig. SI2 (ESI†) shows a systematic representation of the catalyst and GDE preparation.

CO_2 electroreduction set-up

The electrocatalytic tests were carried out using a compact H-type electrochemical cell.[35] The cell is shown in Fig. SI3 (ESI†), and included a current collector made of stainless steel with a built-in spiral flow field, which connected the cathode compartment and the GDE of the cell and guaranteed homogeneous distribution of the inlet reactants. In the first series of experiments, the influence of the promoter phase (CeO_2) was investigated using a CO_2 flow rate of 200 mL min^{-1}, which was adjusted by a manual flow meter (FR2000, Key Instruments). The working gas diffusion electrodes had a projected area of 1 cm^2 to the 1 M KOH aqueous electrolyte, while a platinum square mesh of 1 × 1 cm^2 was used as the counter electrode, located at the anode compartment and separated from the catholyte compartment by a proton exchange membrane (PEM, Nafion® 115) and immersed in 1 M KOH aqueous electrolyte. The total volume of the electrolyte was 150 mL. The reference electrode was an Hg/HgO (1 M NaOH) electrode. The potential values were then translated into RHE (reversible hydrogen electrode) voltages by using eqn (1) and verified by a hydrogen reference electrode (Hydroflex®(M-v01-0071)).

$$E(vs.\ \mathrm{RHE}) = E\left(vs.\ \frac{\mathrm{Hg}}{\mathrm{HgO}}\right) + 0.14\ \mathrm{V} + 0.059\ \mathrm{V} \times \mathrm{pH} \quad (1)$$

For each electrode, the faradaic efficiency (FE) was evaluated by varying the current density from −50 to −300 mA cm^{-2} (Δj = −50 mA cm^{-2}) and using cronopotentiometry (PGSTAT204, Metrohm-Autolab). At each current density, the presence of gas products from the cathode outlet stream was examined for 5 minutes. During this time, the volume of the outlet products was measured and then analysed using an on-line gas chromatography (Shimadzu GC 2030) equipped with a Porapak Q 80/100 column. The gases (H_2, CO, CH_4 and C_2H_4) were detected using a thermal conductivity detector (TCD) and a flame ionization detector (FID).

After the identification of the most promising Ce-promoted copper-based GDE, the influence of the KOH concentration (0.1 M–3 M) and electrolyte type (KCl, KOH, $KHCO_3$,) over the optimized Cu_2O–$5CeO_{2\text{-}C}$ GDE was additionally investigated to find the most effective electrolyte conditions. Finally, a stability test was performed at the selected reaction conditions (j = −250 mA cm^{-2}, electrolyte = 1 M KOH, F_{CO_2} = 200 mL min^{-1}).

The FE_X of the X obtained products, such as C_2H_4, CH_4, CO and H_2, were estimated by using the following equation (eqn 2):

$$\mathrm{FE_X} = \frac{Q_X}{Q_{\mathrm{Total}}} = \frac{n_X N_X F}{Q_{\mathrm{Total}}} \quad (2)$$

where Q_X and Q_{Total} are the charge passed to produce product X and the total passed charge (C) during CO_2RR, n_X represents the electron transfer number of product X, N_X is the product amount (mol) of X measured by the GC, and F is the Faraday constant (96 485 C mol^{-1}).

Catalyst characterization

The series of catalysts sprayed on the carbon-based gas diffusion layer were characterized by different physico-chemical techniques like scanning electron microscopy-energy dispersive X-ray spectroscopy (SEM-EDX), transmission electron microscopy (TEM), X-ray diffraction (XRD), and Raman and photoelectron spectroscopy (XPS).

The surface morphology and elemental composition were investigated using a JEOL JSM-7200F high-resolution SEM equipped with an EDX detector (Oxford instruments) and AZtecEnergy software. Prior to EDX analysis, catalysts were fixed over an aluminium holder. Elemental analysis was carried out at 20 kV and restricted to Cu, Ce, and O to avoid inconsistent results. TEM images were recorded on a FEI Tecnai T12 electron microscope operating at 120 kV. The powder samples were dispersed by ultrasound in ethanol. Suspension drops were deposited on a holey carbon-coated copper grid of 300 mesh and then dried in air.

The crystal structure of the catalysts was examined using a Bruker type XRD D2 Phaser diffractometer. X-ray powder

diffraction patterns were acquired by applying a Cu Kα radiation (λ = 1.5406 Å), a voltage of 40 kV, and a current of 40 mA. Continuous scans were collected over the 2θ range of 10° to 80°. The crystalline phases present in the samples were identified by comparison with reference patterns available in the JCPDS database. The crystallite sizes of the main Cu^x species (Cu_2O, CuO and Cu^0) and cerium oxide (CeO_2) were estimated using the Scherrer's equation at 2θ = 36.46° for Cu_2O (111), 38.76° for CuO (111), 43.32° for Cu (111), and 28.53° for CeO_2 (111); $D = (K\lambda/\beta\cos\theta)$, where λ is the X-ray wavelength, β is the full width of the diffraction line at half maximum (FWHM), and θ is the Bragg angle.

Raman measurements were recorded on a Raman spectrometer (Horiba LabRAM HR800) equipped with a CCD detector, using a laser with a wavelength of 532 nm as the excitation source. The Raman spectra were obtained using a x50LWD objective with an incident power of 0.1 mW (5 acquisitions, 60 s of exposure time).

X-ray photoelectron spectroscopy (XPS) experiments were performed in a PHI 5500 Multitechnique System (from Physical Electronics) with a monochromatic X-ray source (Al Kα 1486.6 eV).

Results and discussion

Characterization

SEM images displayed in Fig. SI4 (ESI†) evidenced that the formation of particles with cubic-like morphology was achieved for both the active phase (Cu_2O) and promoter phase ($CeO_{2\text{-}C}$) prepared at 240 °C. In the case of $CeO_{2\text{-}R}$ prepared at 80 °C, its morphology was not possible to identify by SEM because the particle sizes were below the detection limits. When the electrocatalysts were synthetised in the presence of $CeO_{2\text{-}C}$, a catalytic system composed of particles with a cubic shape was also achieved for the series of $CeO_{2\text{-}C}$-promoted Cu_2O-based catalyst. Furthermore, EDX analysis performed over all catalysts proved the presence of their main components (Cu, Ce, and O). As a representative example, the EDX elemental mapping image exhibited in Fig. 1 demonstrated the experimental composition (82 wt% Cu, 5 wt% Ce, and 13 wt% O) and interaction between the cubic particles of the Cu_2O–$5CeO_{2\text{-}C}$ catalyst.

A summary of the elemental composition of all the as-prepared catalysts is shown in Table 1. The experimental composition of the CeO_2 promoter phase falls within the range of 6–21 wt% ± 1, which closely matches the theoretical values. On the other hand, a slight difference in the elemental composition was mainly identified between the two synthesized promoters ($CeO_{2\text{-}R}$ (81 wt% Ce and 19 wt% O) and $CeO_{2\text{-}C}$ (83 wt% Ce and 17 wt% O)), suggesting the possible presence of different oxidation state of cerium (Ce^{3+} and Ce^{4+}) over these samples. Therefore, the used temperature for the synthesis of CeO_2 nanoparticles can be a key parameter for the generation of Ce^{3+} and Ce^{4+}.

The cubic-like morphology of the $CeO_{2\text{-}C}$ promoter (Fig. 2(a)) and pristine Cu_2O (Fig. 2(b)) was additionally confirmed by TEM. Regarding the $CeO_{2\text{-}R}$, rod-like morphologies with particle sizes of ~8 nm and irregular length can be identified, see Fig. SI5 (ESI†). Between cubic particles, the main difference observed was the size. The cubic $CeO_{2\text{-}C}$ particles (~29 nm)

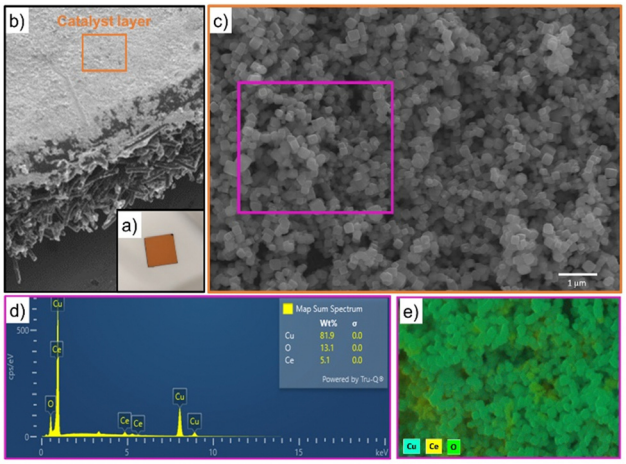

Fig. 1 Surface morphology and elemental composition analysis for the Cu_2O–$5CeO_{2\text{-}C}$ GDE. (a) Image of the as-prepared GDE. (b) SEM image showing the catalyst layer and the carbon-based GDL. (c) SEM image of the electron micrograph region, (d) EDX spectrum, (e) and distribution of Cu, Ce and O in elemental mapping.

Table 1 Elemental composition of the catalysts

	Elemental composition		
	Cu	Ce	O
Sample		[wt% ±2]	
Cu_2O	89	—	11
Cu_2O–$5CeO_{2\text{-}C}$	82	5	13
Cu_2O–$10CeO_{2\text{-}C}$	75	9	16
Cu_2O–$15CeO_{2\text{-}C}$	70	12	18
Cu_2O–$20CeO_{2\text{-}C}$	62	17	21
$CeO_{2\text{-}C}$	—	83	17
$CeO_{2\text{-}R}$	—	81	19
Cu_2O–$5CeO_{2\text{-}R}$	81	4	15

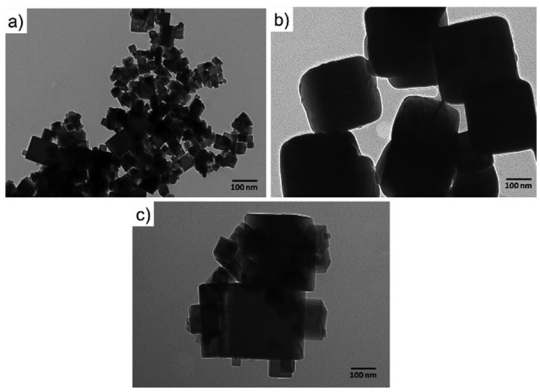

Fig. 2 TEM images of the (a) $CeO_{2\text{-}C}$, (b) Cu_2O, and (c) Cu_2O–$5CeO_{2\text{-}C}$ catalysts.

were smaller than cubic Cu_2O particles (~165 nm). The interaction between the $CeO_{2\text{-}C}$ and Cu_2O particles was clearly detected over a series of Cu_2O–$CeO_{2\text{-}C}$ catalysts. Fig. 2(c) is an example of the strong Cu_2O–CeO_2 interaction achieved over the Cu_2O catalyst promoted by 5 wt% $CeO_{2\text{-}C}$. For this $CeO_{2\text{-}C}$-promoted Cu_2O catalyst, a decrease in the Cu_2O particle sizes was found, suggesting that the addition of CeO_2 during the synthesis inhibits the growth of Cu_2O particles. The average particle sizes estimated for $CeO_{2\text{-}C}$ and Cu_2O were 43 nm and 160 nm, respectively.

The XRD patterns of the $CeO_{2\text{-}C}$ promoter, pristine Cu_2O and the series of $CeO_{2\text{-}C}$-promoted Cu_2O are shown in Fig. 3. The XRD profiles confirmed the phase purity of the polycrystalline CeO_2 (JCPDS: 00-034-0394) and Cu_2O (JCPDS: 00-005-0667). For the $CeO_{2\text{-}C}$ sample, the high-intensity reflections are observed at 2θ = 28.53, 33.09, 47.48, 56.33, 59.08, 69.41, 76.69, and 79.04° corresponding to the CeO_2 (111), (200), (220), (311), (222), (400), (331), (420) lattice planes. On the other hand, the diffraction peak at around 2θ = 29.61, 36.46, 42.34, 61.42, and 73.56° represent the Cu_2O (110), (111), (200), (220), and (311) lattice planes. Over the series of Cu_2O–$CeO_{2\text{-}C}$ catalysts, CeO_2 and Cu_2O reflections were identified at a similar 2θ position, but with differences in their relative intensity, in agreement with the composition. With higher CeO_2 content, the intensity of the reflections of CeO_2 increased, while the reflections of Cu_2O were decreased. Compared to $CeO_{2\text{-}C}$ promoter, the XRD profiles of $CeO_{2\text{-}R}$ suggested that the sample appeared to be composed of small particles. Only four reflections were identified for the $CeO_{2\text{-}R}$. As can be seen in Fig. SI6 (ESI†), the reflections related to CeO_2 phase in the Cu_2O–$CeO_{2\text{-}R}$ were under the detection limit. These reflections were identified at 2θ = 28.53, 33.09, 47.48, 56.33° and associated to the CeO_2 (111), (200), (220), (311) lattice planes.

On the other hand, Raman spectroscopy analysis was additionally performed over the most promising fresh samples ($CeO_{2\text{-}C}$, Cu_2O, and Cu_2O–$5CeO_{2\text{-}C}$) taking into consideration that the formation of defective sites can be interpreted by the alteration in M–O vibration frequency after CeO_2 introduction to the Cu_2O structure. Fig. 4 proved that the fluorite-type cubic

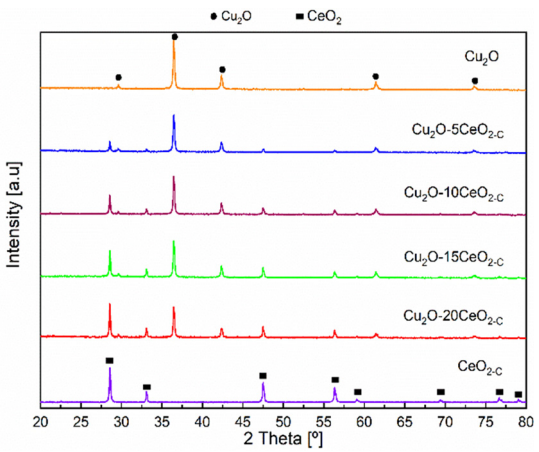

Fig. 3 XRD Patterns of the catalysts.

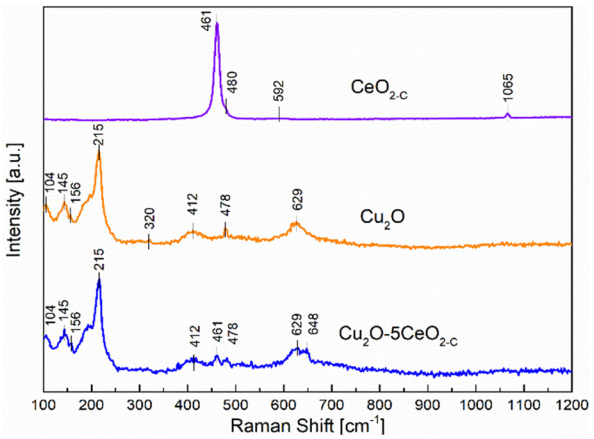

Fig. 4 Raman spectrum of $CeO_{2\text{-}C}$, Cu_2O and Cu_2O–$5CeO_{2\text{-}C}$ catalysts.

crystal structure of ceria in the $CeO_{2\text{-}C}$ sample exhibits one first-order Raman active fundamental mode located at 461 cm^{-1}.[36] This F_{2g} mode was associated with the symmetric vibrations of oxygen ions around Ce^{4+} ions in octahedral Ce–O_8.[37] The bands at 480 and 592 cm^{-1} were attributed to the oxygen vacancies due to the presence of reduced Ce^{3+} cations ($Ce^{3+}O_8$)[38] and the vacancy-interstitial Frenkel-type oxygen intrinsic defects in pure ceria,[39] respectively. Additionally, solid-state phonons assigned to second-order features 2ωR(X) were observed at 1065 cm^{-1}.[40]

In the non-promoted Cu_2O sample, the most intense Raman peak identified at 215 cm^{-1} was related to the second-order overtone $2\Gamma_{12}^-$.[41] The remaining Raman bands were assigned as follows: an inactive mode Γ_{12}^- at 104 cm^{-1}, an IR active mode $\Gamma_{15}^{(1)}$ (LO) at 145 cm^{-1}, a fourth order overtone $4\Gamma_{12}^-$ at 412 cm^{-1}, and an IR active mode $\Gamma_{15}^{(1)}$ (TO) at 629 cm^{-1}.[42–44] In addition to the prominent peaks observed for Cu_2O, a weak band was also observed at 320 cm^{-1}, which corresponds to the A_g mode of CuO.[45] On the other hand, the introduction of CeO_2 into the Cu_2O structure induced the formation of a new extrinsic MO_8 site capable of delivering oxygen under reducing conditions, *i.e.* part of a Frenkel defect.[46] This new Raman peak identified over the Cu_2O–$5CeO_{2\text{-}C}$ catalyst located at 648 cm^{-1} can be probably an effect of the strong interaction between Cu^+ and Ce^{3+} cations.[47] Furthermore, the presence of the CuO phase was not identified in comparison with the Cu_2O sample, implying that CeO_2 avoids overoxidation of Cu_2O and preserves the Cu(I) oxidation state.

The surface elemental composition and chemical state of the fresh $CeO_{2\text{-}C}$, Cu_2O and Cu_2O–$5CeO_{2\text{-}C}$ samples were examined by X-ray photoelectron spectroscopy. The survey scan in Fig. SI7 (ESI†) shows the presence of C, Cu, Ce and O. The C 1s peak at 284.4 eV was used as a reference peak for calibration of all the spectra. The high-resolution XPS spectra of Cu 2p are presented in Fig. 5. The peaks at 932.1 eV and 951.9 eV were linked to Cu^+ $2p_{3/2}$ and Cu^+ $2p_{1/2}$, respectively. Furthermore, characteristic shoulder peaks can also be resolved at 934.8 and 954.8 eV, which were associated with Cu^{2+} $2p_{1/2}$ and Cu^{2+} $2p_{3/2}$, respectively. The presence of satellite peaks at the binding

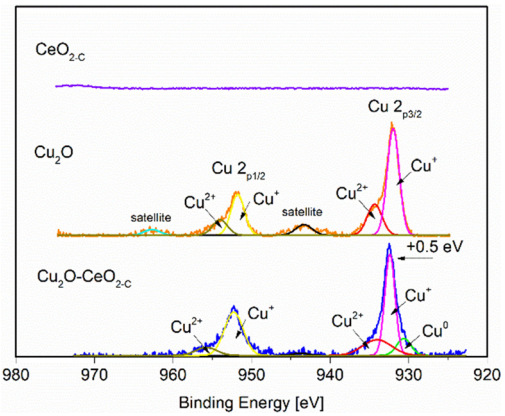

Fig. 5 Cu2p XPS spectra of $CeO_{2\text{-}C}$, Cu_2O and Cu_2O–$5CeO_{2\text{-}C}$ catalysts.

energies of 943.4 indicated that Cu(I) was the major valence state for Cu species.[48]

The peaks of the Cu_2O–$5CeO_{2\text{-}C}$ nanocomposites shift in the direction of high binding energy compared with that of the Cu_2O nanocrystals. The difference between the two peaks is 0.5 eV from the binding energy, which indicates that there is an electronic exchange between Cu_2O and CeO_2. In particular, the Cu^0 phase was identified in the Cu_2O–$5CeO_{2\text{-}C}$ sample, suggesting that CeO_2 promotes the reduction of CuO. Regarding the CeO_2 phase (see Fig. SI8, ESI†), peaks at 881.9, 888.1, 897.9, 899.8, 901.8, and 916.1 eV were only detected in the Ce 3d spectrum of the CeO_2 sample, corresponding to the binding energies of Ce^{4+} $3d_{5/2}$, Ce^{3+} $3d_{5/2}$, SU_1, Ce^{4+} $3d_{3/2}$, SU_2, and Ce^{3+} $3d_{3/2}$, respectively.[49] Fig. SI9 (ESI†) depicts the high-resolution O 1s spectra of the different catalysts. The characteristic peaks resolved in the binding energy range of 534.6 to 526.3 eV were assigned to lattice oxygen (O_{lat}) and oxygen vacancies (O_{Vs}).[50,51] Compared to Cu_2O, the relative proportion of oxygen vacancies was higher for the Cu_2O–$5CeO_2$. The Ov_s are renowned for their possession of weakly bound electrons, serving as exceptional Lewis base sites for CO_2 adsorption. These electrons contribute to the formation of the $CO_2^{\bullet-}$ intermediate by providing electron donation.[52,53] Therefore, this indicates that the Cu_2O–$5CeO_2$ exhibits the strongest ability for CO_2 adsorption and subsequent electrochemical reduction.

CO_2RR

CeO_2 loading. Fig. 6 illustrates the influence of $CeO_{2\text{-}C}$ loading on a series of Cu_2O-based gas diffusion electrodes (GDEs). During the CO_2 electroreduction reaction in 1 M KOH, the main products detected across all GDEs were C_2H_4, CH_4, CO, and H_2. Within the evaluated range of current densities (−50 to −300 mA cm^{-2}), the faradaic efficiencies for C_2H_4 production were consistently higher in the $CeO_{2\text{-}C}$-promoted Cu_2O-based GDEs compared to the non-promoted

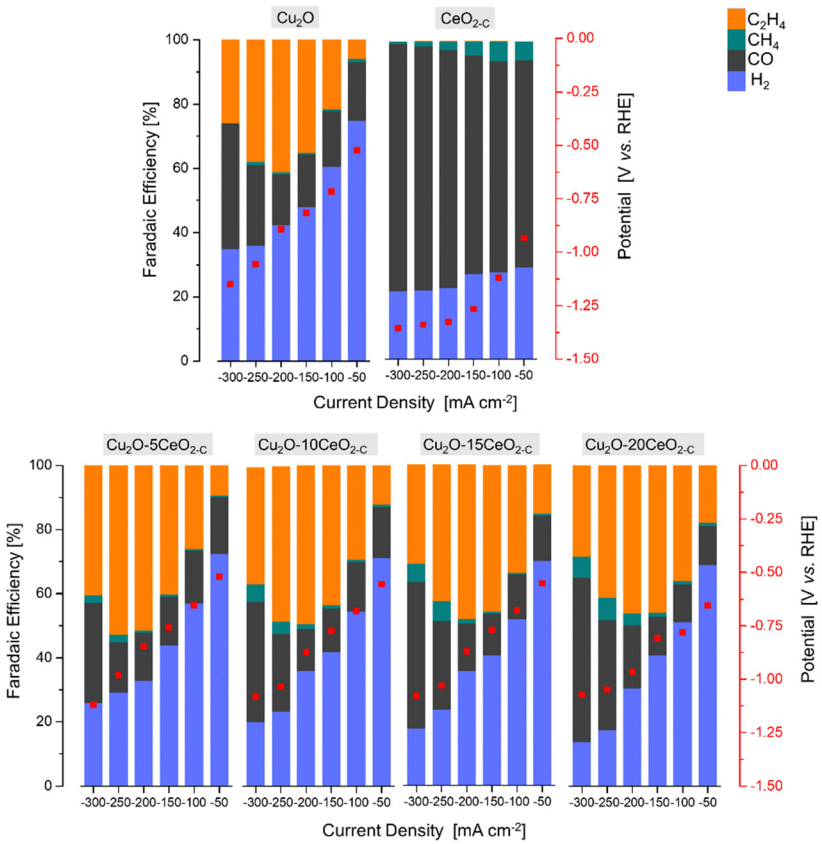

Fig. 6 The faradaic efficiency [%] and potential [V *vs.* RHE] as a function of the current density [mA cm^{-2}] over the series of Cu_2O-based GDEs.

Cu_2O GDE. This indicates that the incorporation of the $CeO_{2\text{-}C}$ promoter phase is beneficial for enhancing C_2H_4 formation during the CO_2RR.

The product formation on the $CeO_{2\text{-}C}$ electrode starts at approximately −0.93 V *vs.* RHE, see Fig. 6. The achieved faradaic efficiencies (FEs) for C_2H_4 were lower compared to the FEs for other sub-products such as H_2, CO, and CH_4. The maximum $FE_{C_2H_4}$ observed for this electrode was 0.6% at −1.34 V *vs.* RHE, and this was achieved at a high current density (j = −250 mA cm^{-2}). In contrast, when the current densities exceeded −150 mA cm^{-2}, a noticeable increase in FE_{CO} (>75% at −1.33 V *vs.* RHE) and a decrease in FE_{CH_4} (<3% at −1.33 V *vs.* RHE) were observed. Comparing with the $CeO_{2\text{-}C}$ electrode, the Cu_2O electrode exhibited a maximum $FE_{C_2H_4}$ of approximately 41% at −0.87 V *vs.* RHE, which was achieved at a current density of −200 mA cm^{-2}. The onset potential for C_2H_4 formation (approximately −0.52 V *vs.* RHE) was lower compared to the $CeO_{2\text{-}C}$ electrode.

The observed behaviour of faradaic efficiencies (FEs) for the Cu_2O–$CeO_{2\text{-}C}$ series indicates that a lower amount of the CeO_2 promoter is favoured to enhance C_2H_4 production. In this case, the potential at which C_2H_4 formation starts ranged between −0.52 and −0.67 V *vs.* RHE. It is noteworthy that the maximum FEs for C_2H_4 were shifted towards lower current densities due to the increased CeO_2 loading. Furthermore, the FE_{CO} and FE_{CH_4} increased, while FE_{H2} decreased with both increasing CeO_2 loading and current density. Among the Cu_2O–$CeO_{2\text{-}C}$ electrodes, Cu_2O with 5 wt% of $CeO_{2\text{-}C}$ was determined to be the optimum electrode for C_2H_4 production. It achieved a maximum $FE_{C_2H_4}$ of approximately 53% at −0.98 V *vs.* RHE, at a current density of −250 mA cm^{-2}.

To investigate the influence of the CeO_2 particle morphology, a CO_2RR test was conducted using rod-like ceria particles ($CeO_{2\text{-}R}$) with the optimized promoter content of 5 wt% (previously found for cubic-like ceria particles, $CeO_{2\text{-}C}$), under the same reaction conditions (1 M KOH, j = −50 to −300 mA cm^{-2}). Fig. SI10 and SI11 (ESI†) revealed that the FEs for C_2H_4 formation are dependent on the shape of the promoter particles.

In the $CeO_{2\text{-}R}$ promoter electrode, the main products observed were CO, H_2, CH_4, and C_2H_4, similar to the $CeO_{2\text{-}C}$ promoter. However, compared to $CeO_{2\text{-}C}$, the $CeO_{2\text{-}R}$ electrode required a more negative potential (−0.94 V *vs.* RHE) to initiate C_2H_4 formation. Furthermore, the maximum FE for C_2H_4 (∼0.15% at −1.26 V *vs.* RHE) over $CeO_{2\text{-}R}$ was detected at a current density of −150 mA cm^{-2}. This suggests that the rod-like ceria morphology is less favourable for C_2H_4 production, as a higher potential was achieved at relatively low current densities. Regarding the FEs for other subproducts, $CeO_{2\text{-}R}$ exhibited a lower FE for CO and higher FE for H_2 and CH_4 compared to $CeO_{2\text{-}C}$, as shown in Fig. SI10 (ESI†).

On the other hand, the combination of Cu_2O with $CeO_{2\text{-}R}$ did not have a positive effect on enhancing the faradaic efficiency for C_2H_4, see Fig. SI11 (ESI†). The maximum $FE_{C_2H_4}$ achieved over the Cu_2O–$CeO_{2\text{-}R}$ electrode was only ∼50% at −0.90 V *vs.* RHE. This low faradaic efficiency can be attributed to the insignificant promotion of CO_2 and H_2O activation by the presence of $CeO_{2\text{-}R}$, as shown in Fig. SI9 (ESI†). Therefore, the results suggest that $CeO_{2\text{-}C}$ promotes more suitable activation of both CO_2 and H_2O molecules, which is crucial for ensuring the selective formation of C_2H_4. It should be noted that the optimum catalyst exhibits a low cathodic polarization compared to pristine Cu_2O (Fig. SI12, ESI†) attributed to the local CO formation at the $CeO_{2\text{-}C}$ promoter and simultaneous CO_2 and CO electroreduction. Thus, the combination of Cu_2O with $CeO_{2\text{-}C}$ demonstrates improved performance in terms of $FE_{C_2H_4}$ compared to Cu_2O–$CeO_{2\text{-}R}$.

Electrolyte. The influence of three different electrolytes, namely KOH, KCl, and $KHCO_3$, was investigated on the optimized Cu_2O–$5CeO_{2\text{-}C}$ catalyst while maintaining a constant electrolyte concentration of 1 M and varying the current density (j = −[50–300] mA cm^{-2}). In terms of C_2H_4 production, the KOH electrolyte exhibited higher C_2H_4 faradaic efficiencies (≥9% at −0.52 V *vs.* RHE) at all tested current densities, except for 50 mA cm^{-2}. The selectivity trend for C_2H_4 among the

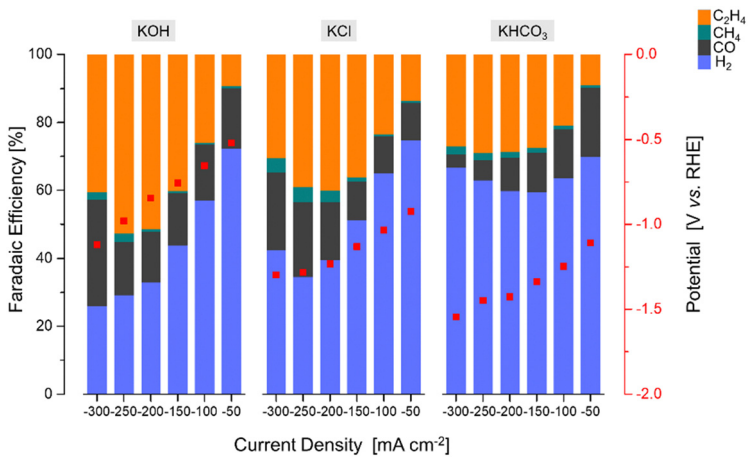

Fig. 7 The faradaic efficiency [%] and potential [V *vs.* RHE] as a function of current density [mA cm^{-2}] over the Cu_2O–$5CeO_{2\text{-}C}$ GDE using different electrolytes.

different electrolytes was observed as follows: KOH > KCl > $KHCO_3$, as shown in Fig. 7. As the current density increased, the preferential occurrence of the hydrogen evolution reaction was observed in the electrolytes based on KCl and $KHCO_3$. Overall, $KHCO_3$ exhibited the most negative potentials (> −1.10 V *vs.* RHE) compared to the other evaluated electrolytes. Therefore, the selection of the electrolyte is crucial for the CO_2 reduction reaction on Cu_2O–$5CeO_{2\text{-}C}$ gas diffusion electrodes, with alkaline KOH conditions enabling preferential C_2H_4 production.

KOH concentration. As the electrolyte pH also plays an important role in the CO_2RR to C_2H_4, the influence of the KOH concentration was evaluated by varying the current density (j = −[50–300] mA cm^{-2}). Fig. 8 demonstrates that the electrochemical activity is highly dependent on the concentration of KOH. Notably, the lowest faradaic efficiencies for C_2H_4 production (≥18% at −0.60 V *vs.* RHE) were observed at the selected KOH concentration of 0.1 M. In contrast, there was an expected decline in the preference for the hydrogen evolution reaction with increasing concentration (>1 M). Similarly, at higher current densities (>250 mA cm^{-2}), the hydrogen evolution reaction became even less preferred. Concerning the potentials, more negative values (−1.05 V *vs.* RHE) were achieved with the increase of the KOH concentration. Particularly, CO and CH_4 were the main products promoted at those high negative potential values.

Stability test. The stability of Cu_2O–$5CeO_{2\text{-}C}$ and Cu_2O catalysts shown in Fig. 9 was used to evaluate the effect of the promoter phase. The tests were conducted under the optimized reaction conditions of j = −250 mA cm^{-2} and 1 M KOH electrolyte, which were found to yield the most promising results for the $CeO_{2\text{-}C}$-promoted Cu_2O gas diffusion electrode (GDE). Under these selected conditions, the Cu_2O–$5CeO_{2\text{-}C}$ electrode exhibited a higher $FE_{C_2H_4}$ (~53% at −0.98 V *vs.* RHE) and maintained its stability over a period of 120 minutes. The faradaic efficiencies for other byproducts (H_2, CO, and CH_4) remained constant throughout the reaction (see Fig. SI13, ESI†).

In contrast, when using non-promoted Cu_2O, the initial $FE_{C_2H_4}$ reached a maximum value of approximately 38% at

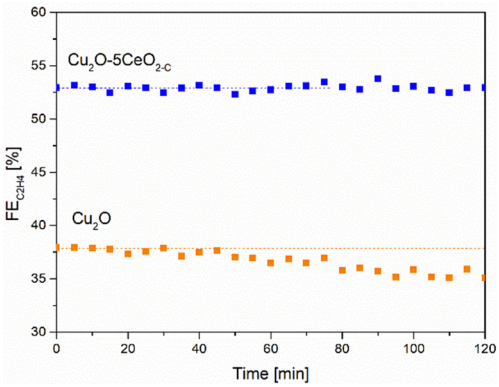

Fig. 9 C_2H_4 FE [%] as a function of the time [min] over the Cu_2O–$5CeO_{2\text{-}C}$ GDE. Reaction conditions: electrolyte = 1 M KOH and j = −250 mA cm^{-2}.

−1.05 V *vs.* RHE but experienced partial deactivation after 45 minutes. The FE for C_2H_4 on the Cu_2O electrode decreased by approximately 5%. Notably, the FEs for CO and H_2 increased as the FE for C_2H_4 and CH_4 decreased on Cu_2O (see Fig. SI14, ESI†).

Consistently with these experimental findings, the 5 wt% $CeO_{2\text{-}C}$-promoted Cu_2O demonstrated enhanced performance compared to the non-promoted Cu_2O electrode in terms of ethylene production, aligning with the results obtained from linear sweep voltammetry (see Fig. SI15, ESI†). The Cu_2O–$5CeO_{2\text{-}C}$ electrode exhibited a more positive onset potential than Cu_2O, indicating that it was the most active catalyst for the CO_2RR.

XRD measurements were also conducted on the Cu_2O and Cu_2O–$5CeO_{2\text{-}C}$ gas diffusion electrodes at different reaction times (t = 0 (before reaction: fresh), 5 and 120 min (after reaction: used)) to investigate the surface copper species during the stability test. In both the fresh and used electrodes, reflections at 18.15, 25.67, and 52.74° were attributed to the carbon phase (JCPDS: 00-047-0787 and 00-026-1076) of the carbon-paper support (see Fig. SI16, ESI†). Prior to sample activation (t = 0 min), characteristic reflections associated with the Cu_2O

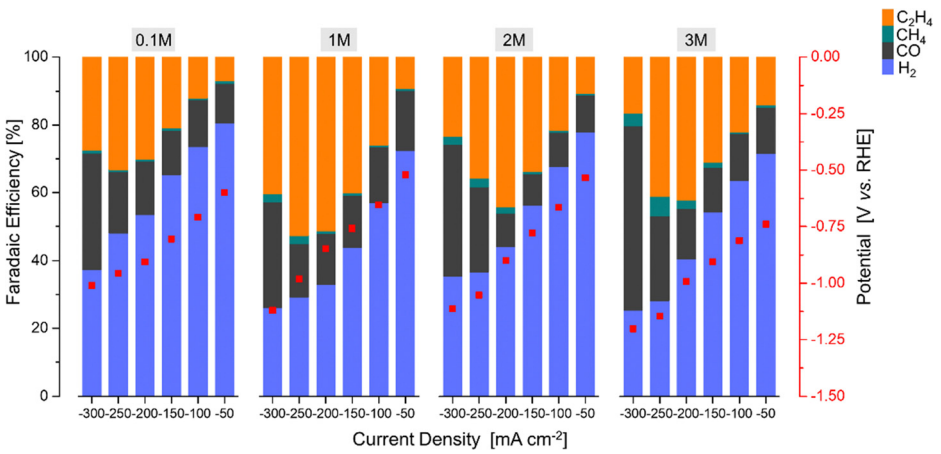

Fig. 8 The faradaic efficiency [%] and potential [V *vs.* RHE] as a function of the current density [mA cm^{-2}] over the Cu_2O–$5CeO_{2\text{-}C}$ GDE using different KOH concentrations.

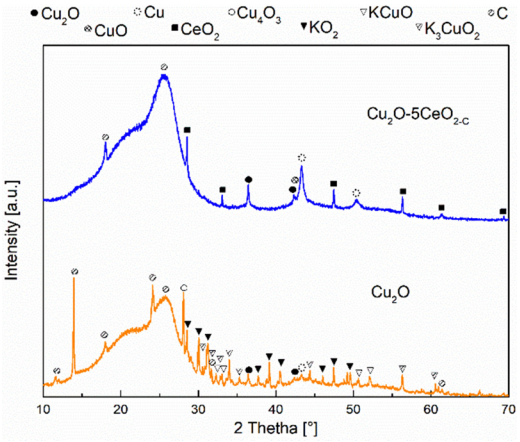

Fig. 10 XRD patterns of the Cu_2O and $Cu_2O-5CeO_2$ GDEs at the reaction time of 120 minutes.

phase were observed in both Cu_2O (see Fig. SI17, ESI†) and Cu_2O–$5CeO_{2\text{-}C}$ (Fig. SI18, ESI†) electrodes. Additionally, CeO_2 was detected on the Cu_2O–$5CeO_{2\text{-}C}$ electrode.

After a reaction time of 5 min, the intensity of reflections corresponding to Cu_2O decreased in both gas diffusion electrodes, and two new phases, CuO (JCPDS: 01-078-0428) and metallic Cu^0 (JCPDS: 00-004-0836), were identified. A similar behaviour was observed for the intensity of the reflections related to the CeO_2 phase in the Cu_2O–$5CeO_{2\text{-}C}$ electrode. However, two new phases, Cu_4O_3 (JCPDS: 00-033-0480) and K_3CuO_2 (JCPDS: 00-038-0971), were specifically identified in the Cu_2O electrode.

At a total reaction time of 120 min (see Fig. 10), the reflections corresponding to CuO phases disappeared, and the intensity of reflections related to Cu_2O and Cu^0 decreased. Additionally, new reflections were observed in the Cu_2O electrode, which were associated with the KCuO (JCPDS: 01-076-2437) and KO_2 (JCPDS: 01-084-1972) phases. In contrast, the reflections of Cu_2O–$5CeO_{2\text{-}C}$ remained like those identified at 5 min, indicating that CeO_2 promoted the stability of the main copper species (Cu_2O, CuO, and Cu^0) involved in the CO_2RR. These identified copper species were consistent with those detected through cyclic voltammetry measurements (see Fig. SI19, ESI†).

According to XRD analysis, the crystallite size of the main Cu^x = Cu^{2+}, Cu^+, and C^0 species were modified after the reaction, see Table SI1 (ESI†). The increase of the Cu_2O crystallite size for the non-promoted Cu_2O catalyst was 15%, while for the Cu_2O–$5CeO_{2\text{-}C}$ it was 1%. For Cu_2O–$5CeO_{2\text{-}C}$, the CeO_2 crystallite sizes were also slightly increased by 8%. Furthermore, the crystallite size corresponding to the Cu phase (20 nm) was higher for the Cu_2O sample. Therefore, the poor stability of the Cu_2O catalyst can result in the increase of the crystallite sizes of the main copper species.

Additionally, SEM-EDS analysis was performed after the reaction to verify the catalyst composition, see Table SI2 (ESI†). Besides the main elements (Cu, Ce, and O), the potassium (K) phase was also detected on the surface of both used catalysts. However, a clear modification of the catalyst composition was identified for used Cu_2O. In this catalyst, the Cu phase decreased by 55% compared to its fresh estate. This behaviour

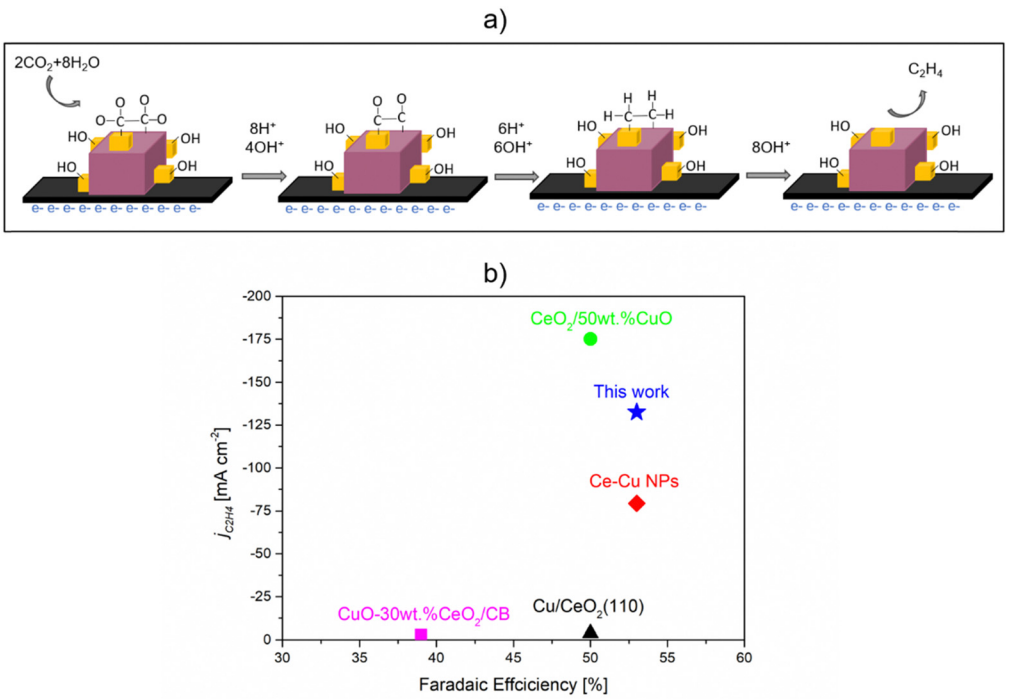

Fig. 11 CO_2RR to ethylene over Cu_2O–$5CeO_2$ GDE. (a) Plausible mechanism of CO_2RR to C_2H_4. (b) Performance comparison with similar catalytic system reported in the literature. 0.1 M $KHCO_3$ was used for CuO-30 wt% CeO_2/CB[31] and Cu/CeO_2(100),[31] while 1 M KOH was used for CeO_2/50 wt% CuO,[33] Ce–Cu NPs,[32] and Cu_2O-5 wt% CeO_2 (this work).

can be related to the presence of the new KOx and KCuOx phases (see Fig. SI20, ESI†), in agreement with post-catalysis XRD results. Regarding the used Cu_2O–$5CeO_2$, its composition was slightly modified, suggesting that $CeO_{2\text{-}C}$ (see Fig. SI21, ESI†) inhibits the formation of potassium species, which are negative for ethylene production.

Based on the electrochemical and catalyst characterization conducted before and after the reaction, it can be concluded that the interaction between Cu_2O and CeO_2 creates intrinsic sites (Cu^x–CeO_{2-x}; Cu^x = Cu^{2+}, Cu^+, Cu^0) for the binding of CO_2 and H_2O. The proposed mechanism, illustrated in Fig. 11(a), suggests that CO_2 can be adsorbed around the Cu^x–CeO_{2-x} interface and reduced to *CO on the CeO_{2-x} site. This step is crucial as CO serves as the key intermediate for the production of C_{2+} products.[30,33] Subsequently, *CO can undergo further reduction to C_2H_4 through enhanced *CO–*CO coupling, which occurs on Cu^x = Cu^{2+}, Cu^+, and Cu^0 sites, with the assistance of H^+ species derived from adsorbed H_2O on Cu^+–CeO_{2-x} sites.[30,54] Therefore, the improved and stable $FE_{C_2H_4}$ achieved with the Cu_2O–$5CeO_{2\text{-}C}$ catalyst supports the assertion that $CeO_{2\text{-}C}$ plays a significant role in the CO_2RR. It promotes the formation of Cu^x–CeO_{2-x} sites, which govern the activity, selectivity, and stability of C_2H_4 production by synergistically activating CO_2 and H_2O molecules.

The performance comparison with catalysts shown in Fig. 11(b), in terms of faradaic efficiency (FE) and partial current density, indicates that Cu_2O–$5CeO_{2\text{-}C}$ is a promising catalytic system for C_2H_4 production. Compared to other reported catalytic systems, Cu_2O–$5CeO_{2\text{-}C}$ demonstrates a high FE for C_2H_4 ($FE_{C_2H_4}$ ~53%) at a high partial current density ($j_{C_2H_4}$ = 132 mA cm^{-2}). Additionally, one of the most significant advantages of Cu_2O–$5CeO_{2\text{-}C}$ is that it requires a lower potential (−0.98 V *vs.* RHE) than the reported CeO_2/50 wt% CuO system (−2.3 V *vs.* RHE) to operate at the same electrolyte concentration of 1 M KOH.[33]

Conclusions

This study investigated the influence of CeO_2 promotion on the catalytic performance of Cu_2O-based catalysts for the electrochemical reduction of CO_2. The addition of the $CeO_{2\text{-}C}$ promoter phase was found to enhance the formation of C_2H_4, a valuable commercial product, during the CO_2RR compared to the non-promoted Cu_2O catalyst. The characterization techniques, including SEM, TEM, XRD, Raman spectroscopy, and X-ray photoelectron spectroscopy, provided valuable insights into the structural and compositional properties of the catalysts.

The results indicated that the synthesized catalysts exhibited well-defined morphologies, with cubic-like particles for Cu_2O and $CeO_{2\text{-}C}$, and rod-like morphologies for $CeO_{2\text{-}R}$. The XRD analysis confirmed the phase of Cu_2O and CeO_2, while Raman spectroscopy revealed characteristic peaks for both materials and a new peak indicating the interaction between Cu^+ and Ce^{3+} cations. X-ray photoelectron spectroscopy further confirmed the presence of different copper oxidation states in the Cu_2O-based catalysts.

The electrochemical evaluation of the catalysts demonstrated that the $CeO_{2\text{-}C}$-promoted Cu_2O-based gas diffusion electrodes (GDEs) exhibited higher faradaic efficiencies for C_2H_4 production compared to the non-promoted Cu_2O GDE. The optimal loading of $CeO_{2\text{-}C}$ for maximum C_2H_4 production was determined to be 5 wt%. The proposed Cu_2O–$5CeO_{2\text{-}C}$ GDE demonstrates enhanced and stable C_2H_4 production through the interaction of Cu_2O and CeO_2, creating active sites (Cu^x–CeO_{2-x}; Cu^x = Cu^{2+}, Cu^+, Cu^0) for the CO_2RR. It exhibits high faradaic efficiency ($FE_{C_2H_4}$ ~ 53%) and partial current density ($j_{C_2H_4}$ = 132 mA cm^{-2}) at a low potential (−0.98 V *vs.* RHE) with 1 M KOH electrolyte, making it a promising catalyst. As an important fact, the FEs for C_2H_4 in the Cu_2O–$5CeO_{2\text{-}C}$ GDE were found to be influenced by the type of electrolyte and its concentration.

These findings highlight the potential of CeO_2 promotion in improving the selectivity and activity of Cu_2O-based catalysts for the CO_2RR. The study contributes to the understanding of the structure–property relationship in CO_2 electrochemical conversion and provides a foundation for further development of more efficient catalysts.

Conflicts of interest

There are no conflicts to declare.

Acknowledgements

This work was funded by AEI projects PID2019-108136RB-C33 and CNS2022-135235 (MCIN/AEI/10.13039/501100011033 and NextGenerationEU/PRTR). A. A. acknowledges the support from the Margarita Salas grant from the European Union – Next Generation EU through the Universitat de Barcelona.

References

1 C. Pappijn, M. Ruitenbeek, M. F. Reyniers and K. Van Geem, *Front. Energy Res.*, 2020, **8**, 557466.
2 G. L. De Gregorio, T. Burdyny, A. Loiudice, P. Iyengar, W. A. Smith and R. Buonsanti, *ACS Catal.*, 2020, **10**, 4854–4862.
3 B. Zhang, J. Zhang, M. Hua, Q. Wan, Z. Su, X. Tan, L. Liu, F. Zhang, G. Chen, D. Tan, X. Cheng, B. Han, L. Zheng and G. Mo, *J. Am. Chem. Soc.*, 2020, **142**, 13606–13613.
4 J. Kim, W. Choi, J. W. Park, C. Kim, M. Kim and H. Song, *J. Am. Chem. Soc.*, 2019, **141**, 6986–6994.
5 D. Tan, J. Zhang, L. Yao, X. Tan, X. Cheng, Q. Wan, B. Han, L. Zheng and J. Zhang, *Nano Res.*, 2020, **13**, 768–774.
6 A. Zahid, A. Shah and I. Shah, *Nanomaterials*, 2022, **12**, 1380.
7 W. Liu, P. Zhai, A. Li, B. Wei, K. Si, Y. Wei, X. Wang, G. Zhu, Q. Chen, X. Gu, R. Zhang, W. Zhou and Y. Gong, *Nat. Commun.*, 2022, **13**, 1877.
8 Y. Jiang, C. Choi, S. Hong, S. Chu, T. S. Wu, Y. L. Soo, L. Hao, Y. Jung and Z. Sun, *Cell Rep. Phys. Sci.*, 2021, **2**, 100356.

9 W. Fu, Z. Liu, T. Wang, J. Liang, S. Duan, L. Xie, J. Han and Q. Li, *ACS Sustainable Chem. Eng.*, 2020, **8**, 15223–15229.
10 W. Lin, H. Chen, Z. Li, K. Sasaki, S. Yao, Z. Zhang, J. Li and J. Fu, *ChemSusChem*, 2021, **14**, 3190–3197.
11 R. M. Arán-Ais, F. Scholten, S. Kunze, R. Rizo and B. Roldan Cuenya, *Nat. Energy*, 2020, **5**, 317–325.
12 Q. Zhu, X. Sun, D. Yang, J. Ma, X. Kang, L. Zheng, J. Zhang, Z. Wu and B. Han, *Nat. Commun.*, 2019, **10**, 3851.
13 Y. Gao, Q. Wu, X. Liang, Z. Wang, Z. Zheng, P. Wang, Y. Liu, Y. Dai, M. Whangbo and B. Huang, *Adv. Sci.*, 2020, **7**, 1902820.
14 J. Bugayong and G. L. Griffin, *ECS Trans.*, 2013, **58**, 81–89.
15 A. Vasileff, C. Xu, Y. Jiao, Y. Zheng and S. Z. Qiao, *Chem*, 2018, **4**, 1809–1831.
16 X. Wang, S. Liu, H. Zhang, S. Zhang, G. Meng, Q. Liu, Z. Sun, J. Luo and X. Liu, *Chem. Commun.*, 2022, **58**, 7654–7657.
17 X. Zhao, H. Xie, B. Deng, L. Wang, Y. Li and F. Dong, *Chem. Commun.*, 2024, **60**, 542–545.
18 J. Wang, Z. Li, C. Dong, Y. Feng, J. Yang, H. Liu and X. Du, *ACS Appl. Mater. Interfaces*, 2019, **11**, 2763–2767.
19 D. Meng, M. Zhang, D. Si, M. Mao, Y. Hou, Y. Huang and R. Cao, *Angew. Chem., Int. Ed.*, 2021, **60**, 25485–25492.
20 T. T. H. Hoang, S. Verma, S. Ma, T. T. Fister, J. Timoshenko, A. I. Frenkel, P. J. A. Kenis and A. A. Gewirth, *J. Am. Chem. Soc.*, 2018, **140**, 5791–5797.
21 I. Merino-Garcia, J. Albo, J. Solla-Gullón, V. Montiel and A. Irabien, *J. CO2 Util.*, 2019, **31**, 135–142.
22 A. Alarcón, J. Guilera, R. Soto and T. Andreu, *Appl. Catal., B*, 2020, **263**, 118346.
23 T. Montini, M. Melchionna, M. Monai and P. Fornasiero, *Chem. Rev.*, 2016, **116**, 5987–6041.
24 F. Wang, M. Wei, D. G. Evans and X. Duan, *J. Mater. Chem. A*, 2016, **4**, 5773–5783.
25 C. Yang, Y. Lu, L. Zhang, Z. Kong, T. Yang, L. Tao, Y. Zou and S. Wang, *Small Struct.*, 2021, **2**, 2100058.
26 S. B. Varandili, J. Huang, E. Oveisi, G. L. De Gregorio, M. Mensi, M. Strach, J. Vavra, C. Gadiyar, A. Bhowmik and R. Buonsanti, *ACS Catal.*, 2019, **9**, 5035–5046.
27 X. Zong, J. Zhang, J. Zhang, W. Luo, A. Züttel and Y. Xiong, *Electrochem. Commun.*, 2020, **114**, 106716.
28 Z. Zhao, X. Li, J. Wang, X. Lv and H. Bin Wu, *J. CO2 Util.*, 2021, **54**, 101741.
29 X. Yan, C. Chen, Y. Wu, S. Liu, Y. Chen, R. Feng, J. Zhang and B. Han, *Chem. Sci.*, 2021, **12**, 6638–6645.
30 S. Chu, X. Yan, C. Choi, S. Hong, A. W. Robertson, J. Masa, B. Han, Y. Jung and Z. Sun, *Green Chem.*, 2020, **22**, 6540–6546.
31 S. L. Chu, X. Li, A. W. Robertson and Z. Y. Sun, *Acta Phys.-Chim. Sin.*, 2021, **37**, 2009023.
32 J. Shan, Y. Shi, H. Li, Z. Chen, C. Sun, Y. Shuai and Z. Wang, *Chem. Eng. J.*, 2022, **433**, 133769.
33 S. Wang, H. Chen, W. Lin, W. Zhou, X. Lv, J. Wang and J. Fu, *Ind. Eng. Chem. Res.*, 2022, **61**, 16445–16452.
34 R. M. Arán-Ais, R. Rizo, P. Grosse, G. Algara-Siller, K. Dembélé, M. Plodinec, T. Lunkenbein, S. W. Chee and B. Roldan Cuenya, *Nat. Commun.*, 2020, **11**, 3489.
35 S. C. Perry, S. M. Gateman, R. Malpass-Evans, N. McKeown, M. Wegener, P. Nazarovs, J. Mauzeroll, L. Wang and C. Ponce de León, *Chemosphere*, 2020, **248**, 125993.
36 S. Loridant, *Catal. Today*, 2021, **373**, 98–111.
37 N. Kainbayev, M. Sriubas, D. Virbukas, Z. Rutkuniene, K. Bockute, S. Bolegenova and G. Laukaitis, *Coatings*, 2020, **10**, 432.
38 C. Schilling, A. Hofmann, C. Hess and M. V. Ganduglia-Pirovano, *J. Phys. Chem. C*, 2017, **121**, 20834–20849.
39 E. Sartoretti, C. Novara, F. Giorgis, M. Piumetti, S. Bensaid, N. Russo and D. Fino, *Sci. Rep.*, 2019, **9**, 3875.
40 R. Zamiri, H. Abbastabar Ahangar, A. Kaushal, A. Zakaria, G. Zamiri, D. Tobaldi and J. M. F. Ferreira, *PLoS One*, 2015, **10**, e0122989.
41 H. Solache-Carranco, G. Juárez-Díaz, M. Galván-Arellano, J. Martínez-Juárez, G. Romero-Paredes and R. Peña-Sierra, in 5th International Conference on Electrical Engineering, Computing Science and Automatic Control (CCE 2008), IEEE, 2008.
42 A. Singhal, M. R. Pai, R. Rao, K. T. Pillai, I. Lieberwirth and A. K. Tyagi, *Eur. J. Inorg. Chem.*, 2013, 2640–2651.
43 A. Sahai, N. Goswami, S. D. Kaushik and S. Tripathi, *Appl. Surf. Sci.*, 2016, **390**, 974–983.
44 C. Lu, Z. Li, L. Ren, N. Su, D. Lu and Z. Liu, *Sensors*, 2019, **19**, 2926.
45 L.-C. Chen, C.-C. Chen, K.-C. Liang, S. H. Chang, Z.-L. Tseng, S.-C. Yeh, C.-T. Chen, W.-T. Wu and C.-G. Wu, *Nanoscale Res. Lett.*, 2016, **11**, 402.
46 M. Dosa, M. Piumetti, S. Bensaid, T. Andana, C. Novara, F. Giorgis, D. Fino and N. Russo, *Catal. Lett.*, 2018, **148**, 298–311.
47 A. Nakajima, A. Yoshihara and M. Ishigame, *Phys. Rev.*, 1994, **50**(18), 13297–13307.
48 Y. Wang, Y. Lü, W. Zhan, Z. Xie, Q. Kuang and L. Zheng, *J. Mater. Chem. A*, 2015, **3**, 12796–12803.
49 Y. Tian, X. Fei, H. Ning, W. Wang, X. Tan, X. Wang, Z. Ma, Z. Guo and M. Wu, *Front. Chem.*, 2022, **10**, 915759.
50 Y. Wang, Y. Lü, W. Zhan, Z. Xie, Q. Kuang and L. Zheng, *J. Mater. Chem. A*, 2015, **3**, 12796–12803.
51 A. Dey, G. Chandrabose, L. A. O. Damptey, E. S. Erakulan, R. Thapa, S. Zhuk, G. K. Dalapati, S. Ramakrishna, N. S. J. Braithwaite, A. Shirzadi and S. Krishnamurthy, *Appl. Surf. Sci.*, 2021, **541**, 148571.
52 Z. Gu, N. Yang, P. Han, M. Kuang, B. Mei, Z. Jiang, J. Zhong, L. Li and G. Zheng, *Small Methods*, 2019, **3**, 1800449.
53 T. Wei, S. Zhang, Q. Liu, Y. Qiu, J. Luo and X. Liu, *Acta Phys.-Chim. Sin.*, 2022, 202207026.
54 Y. Wu, C. Chen, X. Yan, S. Liu, M. Chu, H. Wu, J. Ma and B. Han, *Green Chem.*, 2020, **22**, 6340–6344.